water

MDPI

Article

Research on the Characteristics of Raindrop Spectrum and Its Water Vapour Transport Sources in the Southwest Vortex: A Case Study of 15–16 July 2021

Ting Wang [1], Maoshan Li [1,*], Ming Gong [2], Yuchen Liu [1], Yonghao Jiang [1], Pei Xu [1], Yaoming Ma [3] and Fanglin Sun [4]

[1] School of Atmospheric Sciences, Plateau Atmosphere and Environment Key Laboratory of Sichuan Province, Chengdu Plain Urban Meteorology and Environment Observation and Research Station of Sichuan Province, Chengdu University of Information Technology, Chengdu 610225, China; m13753584206@163.com (T.W.); lyc1848711426020222@163.com (Y.L.); 15814024383@163.com (Y.J.); xupei16@163.com (P.X.)
[2] Meteorological Bureau of Changde City, Changde 415000, China; gongming9799@163.com
[3] Key Laboratory of Tibetan Environment Changes and Land Surface Processes, Institute of Tibetan Plateau Research, Chinese Academy of Sciences, CAS Center for Excellence in Tibetan Plateau Earth Sciences, Beijing 100101, China; ymma@itpcas.ac.cn
[4] Key Laboratory of Land Surface Process and Climate Change in Cold and Arid Regions, Chinese Academy of Sciences, Lanzhou 730000, China; flsun@lzb.ac.cn
* Correspondence: lims@cuit.edu.cn

Abstract: This study investigated the convective weather features, precipitation microphysical characteristics, and water vapour transport characteristics associated with a southwest vortex precipitation event that occurred on the eastern edge of the Qinghai–Tibet Plateau, coinciding with a southwest vortex event, from 15 to 16 July 2021, using conventional observations of raindrop spectra, ERA5 reanalysis data, CMORPH precipitation data, and the HYSPLIT_v4 backward trajectory model. The findings aim to provide theoretical insights for improving the forecasting and numerical simulations of southwest vortex precipitation events. The findings revealed that the precipitation event induced by the southwestern vortex at Emeishan Station on 15–16 July 2021 was characterised by high rainfall intensity and significant precipitation accumulation. The raindrop spectrum exhibited a broad distribution with a notable bimodal structure. Both the Sichuan Basin and the Tibetan Plateau were dominated by the South Asian high pressure at higher altitudes, while a pronounced low-pressure system developed at mid and low altitudes within the basin, establishing a meteorological context marked by upper-level divergence and lower-level convergence. Throughout the event, notable vertical uplift velocities were recorded across the Sichuan Basin and Tibetan Plateau, along with distinct positive vorticity zones in the lower and middle strata of the Sichuan Basin, indicating that the atmosphere was in a state of thermal instability. The majority of moisture was in the mid and lower troposphere with evident convergence movements, which played a crucial role in the southwest vortex's development. WRF numerical simulations of the Emeishan precipitation event more accurately modelled the weather conditions for this precipitation but tended to overestimate the level of precipitation. It was observed that the region around Emei Mountain primarily received moisture influx from the southern Bay of Bengal and the South China Sea, with moisture transport chiefly originating from the Sichuan Basin and in a south-westward trajectory.

Keywords: southwest vortex; raindrop spectrum; weather background; numerical simulation; water vapour transport

check for updates

Citation: Wang, T.; Li, M.; Gong, M.; Liu, Y.; Jiang, Y.; Xu, P.; Ma, Y.; Sun, F. Research on the Characteristics of Raindrop Spectrum and Its Water Vapour Transport Sources in the Southwest Vortex: A Case Study of 15–16 July 2021. *Water* **2024**, *16*, 837. https://doi.org/10.3390/w16060837

Academic Editor: Athanasios Loukas

Received: 15 February 2024
Revised: 9 March 2024
Accepted: 12 March 2024
Published: 14 March 2024

Copyright: © 2024 by the authors. Licensee MDPI, Basel, Switzerland. This article is an open access article distributed under the terms and conditions of the Creative Commons Attribution (CC BY) license (https://creativecommons.org/licenses/by/4.0/).

1. Introduction

The southwestern vortex (SWV) is an α mesoscale closed low-pressure system (low pressure with a closed isobar at 20–200 km) with cyclonic circulation (airflow rotating counterclockwise) at 700 hPa (or 850 hPa) over the southwestern region of China under

the influence of the complex and large topography of the Tibetan Plateau, with a scale size of about 300–500 km [1–4].The southwest vortex occurs in all months of the year, mostly in April–September, and the chance of the southwest vortex moving out of its source is greatest in May–August [5]. Because the southwest vortex often cooperates with the low-level rapids to the east with a large amount of water vapour, the southwest vortex in a place does not move, and it will have an impact on the region in terms of the formation of cloudy and rainy weather. When it moves eastward, it can cause heavy rainfall in southwestern China, as well as in northeastern, eastern, and southeastern China (e.g., Hunan [6]), causing floods, landslides, and other natural disasters, which can result in huge losses and casualties in the local area. When it cooperates with the plateau vortex moving out of the Tibetan Plateau or the subtropical high pressure in the western Pacific Ocean, it can trigger heavy precipitation weather in Sichuan, Chongqing, and their downstream areas in China [7–9]. In terms of the intensity, frequency, and extent of heavy rainfall caused by the southwestern vortex, it is second only to typhoons [10], and it even has the potential to develop into a typhoon as it moves eastward [11].The southwest vortex has played an important role in a number of heavy rainfall events and is the main influence system for the semi-annual heavy rainfall in summer in China [12]. Therefore, revealing the characteristics of the southwest vortex activity, especially in the summer when heavy rainfall is high, is of great practical application value for the improvement of precipitation forecasting in China.

In recent years, meteorologists have carried out a lot of analyses and studies on the southwest vortex and have achieved some research results. Li [13], based on a large number of individual cases analysed by previous authors, found that the scourge of the southwest vortex has three large-scale vortex sources, namely, Jiulong in the southern part of the western Sichuan Plateau, Xiaojin in the central part of the Plateau, and the Sichuan Basin. Lai et al. [14] made a systematic exposition of the spatial and temporal distribution characteristics of the southwest vortex activity and its impact, etc., pointing out that the southwest vortex has two identification methods: manual identification and algorithmic identification, but the algorithmic identification still has the problem of misreporting and the omission of reports. In addition to comprehensive and in-depth research on the southwest vortex system and proposing the basic characteristics of the southwest vortex, scholars have also carried out a large number of individual case analysis studies on the southwest vortex system. Therefore, scholars have conducted a large number of case studies to analyse the distribution characteristics, weather impacts, and early warning and forecasting of the southwest vortex system [15–21]. In addition, meteorologists have also carried out a large number of numerical simulation studies on rainstorms triggered by the southwestern vortex, with a view to gaining a more specific understanding of the characteristics of the development of the southwestern vortex. Cheng et al. [22] carried out a numerical simulation study of a southwest vortex rainstorm on 29–30 June 2013 that better simulated the centre of the precipitation and its weather situation. Jiang et al. [23] conducted a numerical simulation study of the southwestern vortex rainstorm weather process on 4 June 2019 using the WRF model and the WRFDA assimilation system, wherein the assimilated information adjusted the variables in the initial field of the model to make the simulation results closer to the real situation. Lu and Li [24] explored the effect of increasing the sub-high intensity in the western Pacific Ocean on an eastward-moving southwest vortex, pointing out that the change of the flow field directly affects the transport of water vapour and irradiation and dispersion, thus influencing the development and evolution of the southwest vortex. Two contributing factors have been found to influence the genesis of the southwest vortex, namely, the latent heat of condensation and the southerly winds and associated water vapour transport [25]. Therefore, the use of reanalysis data to explore the large-scale background conditions and the energy and water vapour conditions of the southwestern vortex can provide a reference for the artificial identification of the southwestern vortex as well as for the forecasting and monitoring of the southwestern vortex strong convective weather.

The raindrop spectral size distribution (DSD) is one of the very important microphysical parameters for the study of precipitation. By processing the raindrop spectral data of precipitation, the microphysical parameters such as raindrop concentration, average diameter, rain intensity, and radar reflectivity can be calculated, which can be used to analyse the precipitation process and its evolving law and characteristics, having a certain theoretical reference value in the study of the microphysical process of precipitation and the development of the precipitation forecasting work. It was found that mountainous areas affect the raindrop spectral size distribution mainly by influencing the raindrop touch-and-go mechanism [26], and the values of microphysical characteristic parameters, such as rainfall intensity and mass-mean diameter, are higher in mountainous regions than in plains [27]. The Tibetan Plateau region, which has a complex and large topography, has a wider raindrop spectrum compared to the plains at the same latitude and in the same season [28]. Gong et al. [29] analysed the characteristics of raindrop spectra at four stations in the eastern rim of the Tibetan Plateau. It was found that the cumulative precipitation at Linzhi and Nagqu stations was dominated by the contribution of precipitation with small grain size and small rainfall intensity, while the cumulative precipitation at Emeishan and Yushu stations was dominated by the contribution of precipitation with large grain size and large rainfall intensity.

The Sichuan Basin is located in the region west of 110° E in China, with the Yunnan–Guizhou Plateau to the south, the Tibetan Plateau to the west, and the Qinling Highlands to the north. The special geographic location and topographic conditions make the basin a rainstorm-prone region in China [30], where heavy rainfalls triggered by the southwest vortex predominate in particular. Therefore, this study selected a heavy rainfall event occurring in the Sichuan Basin from 15 July to 16 July 2021. This precipitation triggered moderate to heavy rainfall over most of the basin, with torrential rainfall and locally heavy rainfall in the seven cities of Guangyuan, Mianyang, Deyang, Chengdu, Ya'an, Meishan, and Leshan. In this paper, this heavy rainfall process triggered by the southwest vortex was studied, and the microphysical characteristics of precipitation, convective weather characteristics, and water vapour transport characteristics of the southwest vortex were analysed. Understanding the characteristics of the raindrop spectral distribution of precipitation during the southwest vortex can increase the understanding of the cloud microphysical processes of precipitation in the southwest vortex; reduce the errors in precipitation estimation by numerical forecasts; and provide important parameters in cloud microphysical parameterisation schemes, radar quantitative precipitation prediction, and artificially influenced weather [31,32]. The use of reanalysis data to explore the large-scale background conditions and energy and water vapour conditions of the southwestern vortex can provide theoretical references for the artificial identification of the southwestern vortex and the heavy rainfall forecast as well as the monitoring and warning of the strong convective weather of the southwestern vortex, as well as providing a scientific basis for the disaster prevention and mitigation work of the relevant departments.

2. Data and Methods

2.1. Observatory Site

Emeishan is at the southeastern edge of the Tibetan Plateau, located on the transition zone between the main body of the Tibetan Plateau and the Sichuan Basin, where the southwest vortex begins to develop [33], so this paper selected the raindrop spectral data from Emeishan Station on 15–16 July 2021 to analyse the raindrop spectral characteristics of the precipitation of the southwest vortex. The observation station was the Emei Mountain Integrated Atmosphere and Environment Observation Experiment Station of the Chengdu University of Information Engineering (29.28° N, 103.6° E, altitude: 937 m). The observation station is shown in Figure 1.

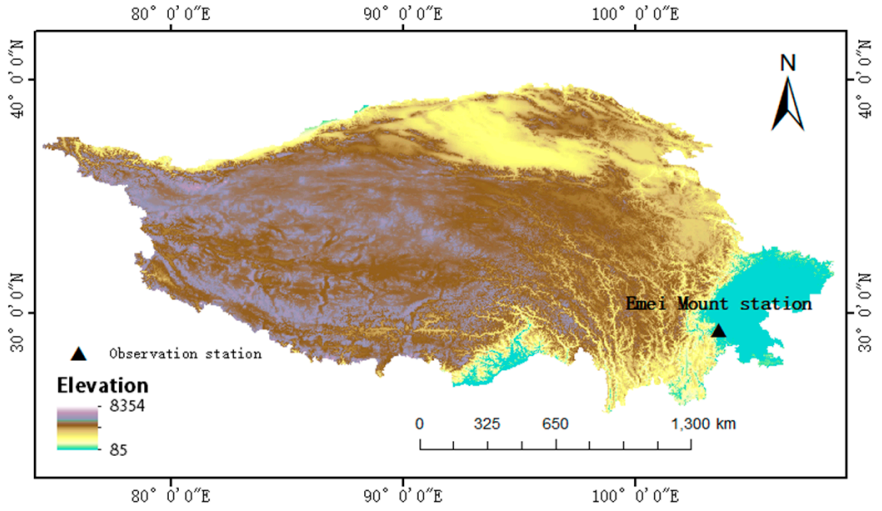


Figure 1. Topography of the study area and location of the observation point.

2.2. Data

(1) Observations from the PS-32 laser raindrop spectrometer at Emeishan Station, Chengdu University of Information Engineering. The data were divided by a laser raindrop spectrometer into 32 channels of observed raindrop spectra according to the size of the equivalent volume diameter and falling speed, which can measure the diameter size and falling speed of precipitation particles, with particle diameter measurements ranging from 0.2 to 25 mm and particle speed measurements ranging from 0.2 to 20 m/s. The average diameter of the smallest precipitation particles within the raindrop spectral data of this study was 0.312 mm due to the exclusion of the first two diameter channels in this study, taking into account the measurement accuracy of the raindrop spectrometer itself.

(2) The European Centre for Medium-Range Weather Forecasts (ECMWF) ERA5 reanalysis information (https://cds.climate.copernicus.eu/cdsapp#!/search?type=dataset, accessed on 18 January 2024 and 14 March 2023).

(3) The Global Data Assimilation Forecasting System (GDAS) used by the National Centers for Environmental Prediction (NCEP) Global Forecasting System (GFS) model in the United States. The GDAS adds the following types of observations to a gridded 3D model space: surface observations, balloon data, wind profiler data, aircraft reports, buoy observations, radar observations, and satellite observations. It can be studied for meteorology, geophysics, and big data (ftp://arlftp.arlhq.noaa.gov/pub/archives, accessed on 10 January 2023).

(4) National Centres for Environmental Prediction (NECP)/National Centre for Atmospheric Research (NCAR) FNL Reanalysis Information (https://rda.ucar.edu/datasets/ds083.2/dataaccess/#, accessed on 24 January 2024).

(5) Global high temporal and spatial resolution CMORPH precipitation data developed by the Climate Prediction Center (CPC) of the United States of America on the basis of a wide range of microwave precipitation data and infrared data, which are suitable for the study of precipitation and its temporal and spatial variability on mesoscale to interannual scales (https://www.ncei.noaa.gov/products/climate-data-records/precipitation-cmorph, accessed on 29 January 2024).

For a detailed description of the usage data, please see Table 1.

Table 1. Detailed data description.

Data Name	Horizontal Resolution	Time Resolution	Data Time Period	Data Content
Raindrop spectrum information	——	1 min	15 July 2021 from 0:00 to 16 July 2021 at 23:00	Data for 32 speed and diameter channels per minute
ERA5	0.25° × 0.25°	1 h	15 July 2021 from 0:00 to 16 July 2021 at 23:00	Potential height, meridional winds, latitudinal winds, specific humidity, etc.
GDAS	——	1 h	2 July to 29 July 2021	——
FNL	1° × 1°	6 h	14 July 2021 12:00 to 17 July 2021 00:00 (Universal Time)	——
CMORPH	0.25° × 0.25°	1 h	15 July 2021 from 0:00 to 16 July 2021 at 23:00	Precipitation data

2.3. Classification of Precipitation Types for Raindrop Spectral Data

Since raindrop spectral data with radar echo intensities below 10 dBZ have very little effect on precipitation, radar reflectivity (Z) data observed by raindrop spectrometers less than 10 dBZ are considered as nonprecipitation data and were excluded in this paper [34]. The classification of precipitation cloud types is based mainly on radar echoes and information obtained from ground-based meteorological observatories. Firstly, based on the shape of the observed clouds, they are simply classified into two types: stratiform and cumulus clouds, which are used to determine whether the precipitation is stratiform or convective precipitation for the duration of the precipitation. In this paper, we referred to the method of Shu et al. [35] to classify the raindrop spectral data into stratocumulus, cumulonimbus, and cumulonimbus mixed cloud precipitation. The basis of judgement is shown in Table 2.

Table 2. Basis for judgement of precipitation cloud types.

Radar Reflectivity (dBZ)	Precipitation Cloud Type
Z > 35	Cumulonimbus precipitation
35 > Z > 30	Cumulus mixed cloud precipitation
Z < 30	Stratocumulus cloud precipitation

2.4. Research Methodology

2.4.1. Calculation of Raindrop Spectral Distribution

Since data greater than 8 mm in the data record is most likely a measurement error, this part of the data was directly excluded. In order to carry out the study and analysis of the characteristics of the raindrop spectrum, it is necessary to solve for the precipitation physical coefficients of the raindrop spectrum. This includes raindrop number concentration N(Di)(m^{-3}), total particle number density N_0, and rainfall intensity R (mm h^{-1}), calculated as follows:

$$\mathrm{N}(D_i) = \sum_{j=1}^{32} \frac{A_{ij}}{V_j \times T \times S} \tag{1}$$

$$N_0 = \sum_{D_i=0}^{D_{max}} N(D_i) \tag{2}$$

$$R = \frac{6\pi}{10^4} \sum_{i=1}^{32} \sum_{j=1}^{32} N(D_i) D_i^3 V_j \Delta D_i \tag{3}$$

where i, j denotes the number of precipitation particles in the i-th diameter channel and j-th velocity channel, respectively; T is the sampling time, T = 60 s; and S is the effective sampling area, S = 54 cm^2.

The parameterisation of raindrop spectra can be described by mathematical models in order to describe the variation of precipitation particle concentration with diameter size

in nature. In this paper, a gamma distribution model was used to fit the raindrop spectral data with the following expression:

$$N(D) = N_0 D^{\mu} \exp(-\lambda D) \quad (4)$$

where N_0 ($m^{-3} \cdot mm^{-1}$) is the concentration parameter, λ (mm^{-1}) is the slope parameter, and μ is the shape parameter.

2.4.2. Water Vapour Flux Calculations

The formula for calculating the water vapour flux in the whole layer is as follows [36]:

$$Q = \frac{1}{g} \int_{ps}^{pt} qVdp \quad (5)$$

where g is the gravitational acceleration, ps is the surface pressure, pt is the upper boundary pressure, q is the specific humidity, and V denotes the wind speed. The whole layer water vapour flux can be written as a latitudinal water vapour flux component and a meridional water vapour flux component:

$$Q = \frac{1}{g} \int_{ps}^{pt} qudp \quad (6)$$

$$Q = \frac{1}{g} \int_{ps}^{pt} qvdp \quad (7)$$

The vertical water vapour flux can be written as

$$Fp = -\omega q, \quad (8)$$

where the vertical velocity can be written as

$$\omega = dp/dt \quad (9)$$

2.4.3. WRF Simulation Programme

In this paper, the WRF-4.3 model was adopted, and the simulation time was from 00:00 on 15 July 2021 to 23:00 on 16 July 2021 (Beijing time, the same below) for 48 h. The model adopts a two-layer nesting, and the simulation centroid is Emeishan Station (29.28° N, 103.6° E); the horizontal direction adopts the Lambert projection, and the horizontal resolutions are 9 km (120 × 120) and 3 km (118 × 118), respectively. The simulation area is shown in Figure 2. The terrain data used were WRF self-contained terrain data of 5 m, 30 s data, with a time step of 54 s, vertically layered with 35 layers.

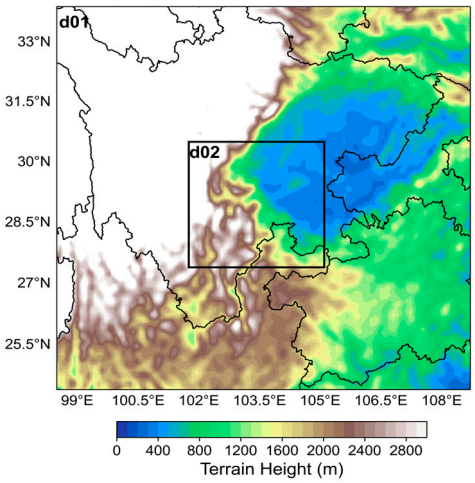


Figure 2. Model area map.

Model scheme design: The Lin scheme was used for the cloud microphysics parameterisation; the rapid radiative transfer model (RRTM) scheme was selected for the longwave radiation scheme, the Dudhia scheme for the shortwave radiation, the Grell–Devenyi scheme for the cumulus cloud parameterisation (used only in the outermost layer of the nesting), the YSU scheme for the boundary layer parameterisation, the Monin–Obukhov scheme for the near-surface layer scheme, and the Noah-MP scheme for the land surface processes.

3. Results

3.1. Characterisation of the Raindrop Spectrum of Precipitation in the Southwestern Vortex on 15–16 July

The altitude of Emeishan Station is 937 m, and its precipitation has strong regional characteristics due to the influence of altitude and topographic factors. The likelihood of collisional fragmentation during raindrop descent in the Emeishan region is smaller than that at high altitudes, so its raindrop spectral concentration has a distribution after particle sizes larger than 7 mm.

Based on accumulated precipitation data from the raindrop spectrometer, the total precipitation at Emeishan Station on 15-16 July reached 67.43 mm, and the average rainfall intensity was 0.75 mm/h. Figure 3a illustrates the raindrop spectrum concentration and gamma fitting chart for Emeishan Station on 15-16 July 2021. It can be clearly seen from the figure that the overall trend of the raindrop spectrum concentration distribution at Emeishan Station was a bimodal distribution, with the first peak occurring at the particle diameter of 0.6 mm, and as the particle diameter increased, the number concentration began to decrease until the particle diameter reached 1.2 mm, where it started to rise again. At a particle diameter of 1.5 mm, the number concentration reached the second peak. Subsequently, the number concentration decreased with increasing particle size. The calculated peak concentration was relatively large, comparable to the summer peak concentration at Emeishan Station. The gamma fitting was better after particle sizes >1.625 mm, with a calculated N_0 value of 295.42 $m^{-3}mm^{-1}$. This indicates that under the influence of the southwest vortex, in terms of the precipitation at Emeishan Station, the rain intensity was stronger and the precipitation amount was also higher, with the width of the raindrop spectral distribution being wider, having a great influence on the raindrop spectral distribution at Emeishan Station.

Figure 3b depicts the raindrop spectrum charts for stratiform clouds, cumulus clouds, and mixed clouds at Emeishan Station on 15–16 July. All three types of cloud precipitation showed an obvious bimodal structure, with peaks at 0.526 mm and 1.375 mm particle size, and the state of its spectrogram was basically consistent with the state of the overall raindrop spectrogram concentration map at Emeishan Station on 15–16 July. Among them, stratiform clouds had the highest peak number concentration; cumulus had the highest peak concentration at 1.375 mm; and cumulus clouds showed the widest spectrum, maintaining a broad distribution even at large particle sizes, with cumulus clouds being the uppermost layer when particle size > 1375 mm, followed by mixed clouds, with stratiform clouds at the bottom, having larger concentrations corresponding to wider spectra.

Figure 3c shows the raindrop spectrum data from Emeishan Station on 15–16 July classified into five different classes according to particle size, in which the largest concentration contribution was made by precipitation particles < 1 mm, which reached 69.5%, followed by particles between 1 and 2 mm, which reached 26.7%. The largest contribution to the precipitation rate was from 1 to 2 mm precipitation particles at 22.3%, and the smallest was from <1 mm precipitation particles, similar to the distribution of particle diameter contributions to precipitation for July–September 2021 at Emeishan Station (figure omitted).

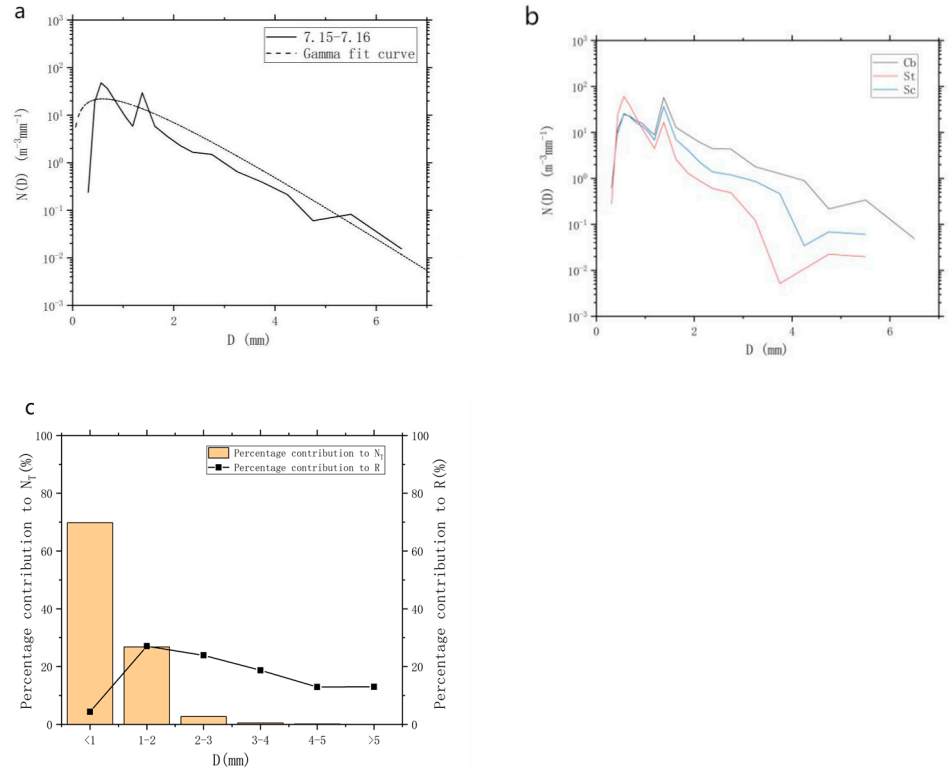


Figure 3. Raindrop spectra and gamma fits for 15–16 July 2021 at Emeishan Station. Raindrop spectra of different precipitation cloud types and particle diameter contribution to concentration NT and rainfall rate R for 15–16 July 2021 at Emeishan Station ((**a**) is the raindrop spectra and gamma fit, (**b**) is the raindrop spectra for different precipitation cloud types, and (**c**) is the contributions).

3.2. Weather Background Analysis

As shown in Figure 4, most of the area temperatures on the 200 hpa altitude map lay in the range of −49 °C to −45 °C. The southwestern part of the Tibetan Plateau is located within the South Asian High, with a geopotential height of 1432 gpm, where the airflow exhibits anticyclonic motion. The South Asian High is active, while the Sichuan Basin is under the control of a high-pressure system ranging from 1428 to 1432 gpm, primarily influenced by northeasterly winds. There is an anticyclone activity in the central Tibetan Plateau on the 500 hpa altitude chart, with the anticyclone centre at 93° E, 35° N. The highest temperature in the western part of the plateau reached 3 °C, and there was a high-pressure centre in the southwestern part of the plateau. The Sichuan Basin is located between the two high-pressure centres, with winds mainly from the north-east and northerly directions, and there was a cyclonic convergence movement in the western part of the Basin (103° E~108° E, 27° N~33° N).

As illustrated in Figure 5a, at 700 hpa, the east-central Tibetan Plateau was mainly controlled by a contour of 356 gpm. There was a high-temperature centre in the Tarim Basin, wherein the airflow engaged in small convective activities, and the highest temperature in the centre was able to reach about 22 °C. In the western part of the Sichuan Basin (103° E~108° E, 30° N~34° N), there was a clear cyclonic convergence motion, and in the northeastern part of the Sichuan Basin, the airflow was in a divergence motion. As shown in Figure 5c, at 08:00 on the 16th, there was a distinct anticyclonic dispersion movement in the central part of the Qinghai–Tibet Plateau on the 500 hPa altitude chart. The graph shows that temperatures were higher in the highlands than in the surrounding areas, with a maximum temperature difference of up to 7 °C. The western part of the Sichuan Basin was consistent with Figure 5a, wherein the airflow exhibited cyclonic convergence movement, with the cyclone range being larger than that at 700 hpa. In connection with Figure 4a, it can be concluded that the western part of the basin is capable of generating upward

movements, providing conditions for precipitation. Figure 5b,d shows that at 20:00, the anticyclonic activity in the central part of the Tibetan Plateau disappeared on the 500 hpa level, and the Tarim Basin remained as a high temperature centre at 700 hpa, with a centre temperature of about 22 °C, but the range of the high temperature was much smaller than at 08:00; the temperature in the east-central and the eastern margins of the Tibetan Plateau were somewhat lower than at 08:00, mostly between 8 °C and 14 °C. At 20:00, there was strong convective activity at 500 hpa and 700 hpa in the northern part of the plateau, and the cyclonic activity disappeared in the western part of the Sichuan Basin. There was evident convective activity at 105° E~108° E and 27° N~31° N, with a predominant northeasterly wind in the central part of the basin. The western and middle parts of the Sichuan Basin were under the control of the high pressure, with a potential altitude of 668 gpm at 500 hpa all the time.

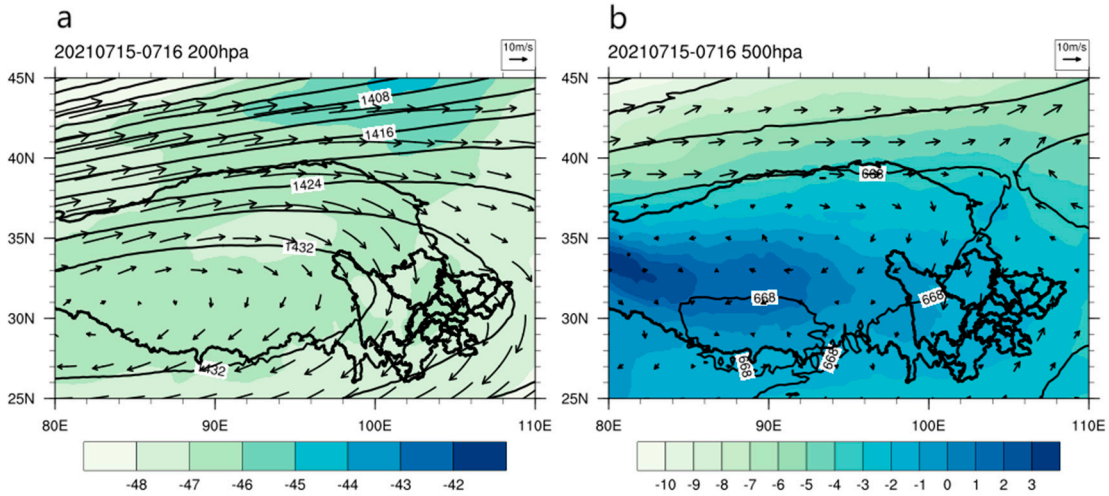


Figure 4. Map of the potential height field from 00:00 on 15 July 2021 to 23:00 on 16 July 2021 ((**a**) is the 200 hpa potential height field, (**b**) is the 500 hpa potential height field, and the black arrows are the wind field maps).

3.3. Energy Analysis

From Figure 6a, it can be seen that the vast majority of the air currents on the eastern edge of the Tibetan Plateau and in the Sichuan Basin area were in an upward motion, with vertical velocities of most airflow reaching above 10 m/s. However, within the range of 80° E to 85° E below 250 hpa and 107° E to 110° E below 700 hpa, the airflow was descending, with vertical velocities around −10 m/s. The upward motion of the airflow was particularly strong in the range from 104° E to 108° E, and there was a clear centre of upward motion between 250 hpa and 350 hpa in this range, with the central vertical velocity reaching 50 m/s. This indicates that the range from 104° E to 108° E was the centre of this precipitation. Figure 6b depicts a vertical velocity profile along 30° N at 08:00 on 16 July 2021. Similar to Figure 6a, most airflow within the observation area underwent upward motion, but the range of flow in a downward motion was not consistent. At 08:00 on the 16th, there was a descending motion above 250 hpa, and an especially strong descending motion was observed between 120 hpa and 160 hpa within the range of 105° to 108° E, with vertical velocities reaching around −15 m/s. At this time, the upward motion of airflow became even more intense, with strong upward motion throughout the entire atmospheric column within the range of 96° E to 98° E. The airflow over the Sichuan Basin alternated between upward and downward motion, especially at the 500 hpa level, wherein the upward and downward motion of airflow was strong, and vertical velocities were very high.

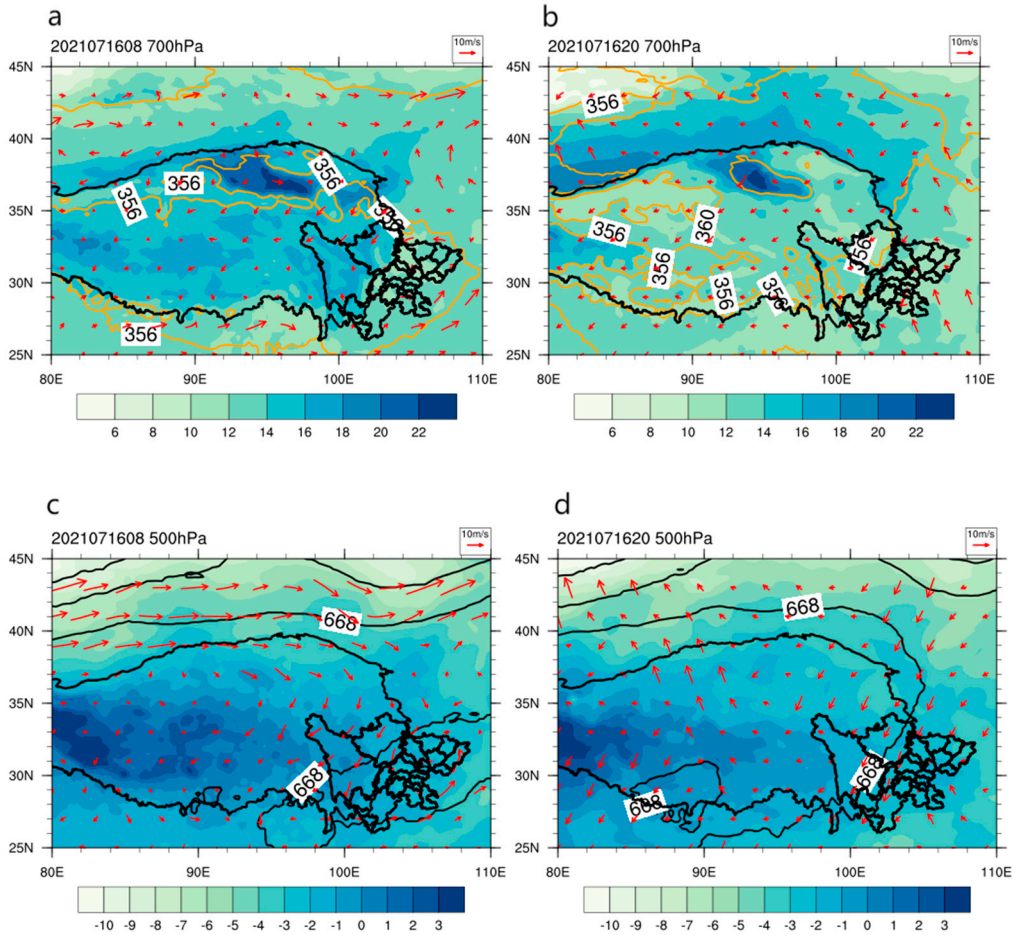


Figure 5. The 500 hpa and 700 hpa potential height field at 08:00 on 16 July 2021, and the 500 hpa and 700 hpa potential height field at 20:00 on 16 July 2021 ((**a**) is the 700 hpa height field at 08:00, (**b**) is the 700 hpa height field at 20:00, (**c**) is the 500 hpa height field at 08:00, (**d**) is the 500 hpa height field at 20:00; the yellow line and black line is the height field, and the red arrows are the wind field diagram).

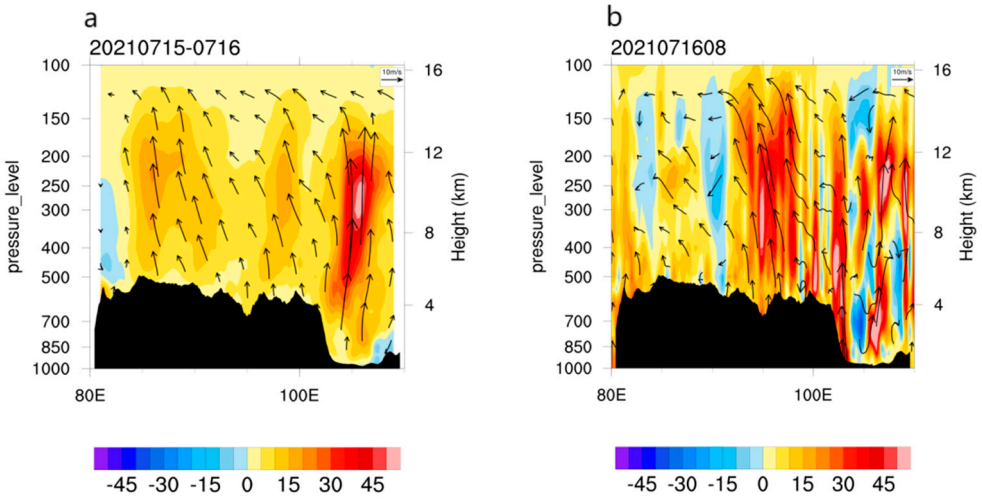


Figure 6. Mean vertical velocity profile along 30° N on 15–16 July 2021. (**a**) Vertical velocity profile along 30° N on 15–16 July 2021; (**b**) vertical velocity profile along 30° N at 08:00 on 16 July 2021 (vector arrows: 10 m/s; topographic maps of the Tibetan Plateau and the Sichuan Basin on the black background).

Figure 7a shows the profile of the equivalent potential temperature along 30° N at 08:00 on 15 July 2021, when the atmosphere was in a thermally stratified unstable state below the 500 hpa altitude layer in the range 102° E to 110° E. Figure 7b shows the profile of relative vorticity along 30° N at 08:00 on 15 July 2021, and it can be seen that the relative vorticity was negative near the 200 hpa altitude layer around 80° E, there was a large relative vorticity between the 600 hpa–450 hpa altitude layer in the range of 101° E to 104° E, and the value of the relative vorticity of the 850 hpa altitude layer in the range of 104° E to 108° E was around 1×10^{-4} s^{-1}. As shown in Figure 7a,b, at 08:00 on the 15th in the Sichuan Basin range in the middle and lower levels, there was the emergence of a clear convergence zone, and the atmosphere was in a state of instability, necessary for the precipitation on the 15th to provide more favourable energy conditions.

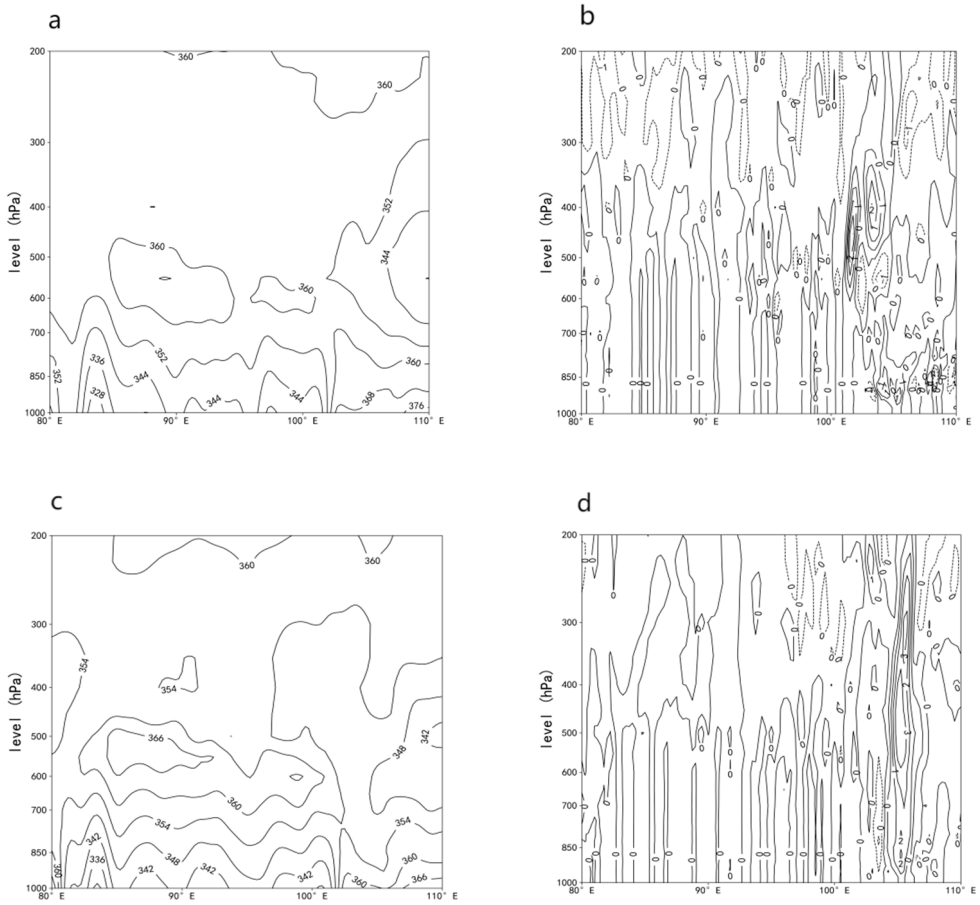


Figure 7. Equivalent potential temperature profile and relative vorticity profile along 30° N at 08:00 on 15 July 2021 and 08:00 on 16 July 2021 ((**a**) the equivalent potential temperature profile at 08:00 on 15 July 2021 (unit: K); (**b**) the relative vorticity profile at 08:00 on 15 July 2021 (unit: 10^{-4} s^{-1}); (**c**) the equivalent potential temperature profile at 08:00 on 16 July 2021 (unit: K); and (**d**) the relative vorticity profile at 08:00 on 16 July 2021 (unit: 10^{-4} s^{-1})).

Figure 7c shows the profile of the equivalent temperature along 30° N at 08:00 on 16 July 2021, from which it can be seen that the atmosphere was in a thermally stratified unstable state between the 500 hpa and 450 hpa altitude layers in the range from 85° E to 95° E and below the 500 hpa altitude layer in the range from 102° E to 110° E. Figure 7d shows the relative vorticity profile along 30° N at 08:00 on 16 July 2021, in which there was no obvious convergence and divergence in most of the area, and the relative vorticity value was close to zero, with the height layer of 600 hpa~450 hpa between 104° E and 106° E having a large relative vorticity value in which the relative vorticity value of the height of 500 hpa reached more than 3×10^{-4} s^{-1}, corresponding to the wind field of 500 hpa and

700 hpa in Figure 5. As shown in Figure 7c,d, at 08:00 on the 16th, the Sichuan Basin range was below the 450 hpa altitude layer for the convergence zone; above the 300 hpa altitude layer for the convergence zone; and the atmosphere was in an unstable state, not only for the occurrence of precipitation to provide a high altitude convergence of the convergence of the dispersal of the weather characteristics of the convergence of the low altitude, providing a favourable energy conditions.

3.4. Analysis of Water Vapour Conditions

Figure 8 shows the vertical profile of specific humidity averaged by longitude and pressure within the range of 25° N to 45° N and 60° E to 115° E from 15 to 16 July 2021. Water vapour concentrations in the study area were relatively small above 500 hpa, with water vapour mainly concentrated below 500 hpa. From the graph, it is evident that specific humidity at 850 hPa to 1000 hPa in the range of 75° E to 80° E was able to reach up to 13 g kg^{-1}, and in the range of 110° E to 115° E, it was able to peak at 16 g kg^{-1}. Above 800 hPa, the average specific humidity in the region of 80° E to 100° E generally maintained around 10 g kg^{-1}. Specific humidity above 400 hPa was mostly between 0 and 2 g kg^{-1}, and the average specific humidity between 400 hPa and 500 hPa was typically within the range of 2 to 4 g kg^{-1}.

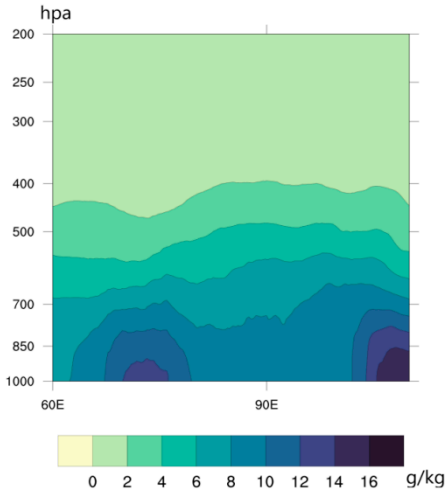


Figure 8. Longitude pressure vertical profile of average specific humidity from 15 to 16 July 2021 (unit: g kg^{-1}).

Figure 9 shows the distribution of water vapour flux on 15–16 July 2021 in the meridional and latitudinal directions. Figure 9a shows that most of the latitudinal distribution of water vapour fluxes over the Tibetan Plateau and the Sichuan Basin within 25°N~35° N had values between −2 and 3 × 10^5 m s^{-1} g kg^{-1}, and that the distribution was basically east–west oriented, which was consistent with the average latitudinal airflow. The water vapour flux was basically distributed in an east–west direction, which was consistent with the distribution of the mean latitudinal airflow. There was a clear negative water vapour flux region in the range of 28° N to 34° N in the figure, which was especially strong in the range of 98° E to 105° E, with a central value of about −2 × 105 m s^{-1} g kg^{-1}. This indicates that water vapour was being transported westwards and was able to provide adequate water vapour conditions for precipitation. In the southeastern part of the Sichuan Basin (28°~31° N, 104~106° E), there was a small positive zone with flux values around 2 × 105 m s^{-1} g kg^{-1}, indicating that water vapour was being transported eastwards.

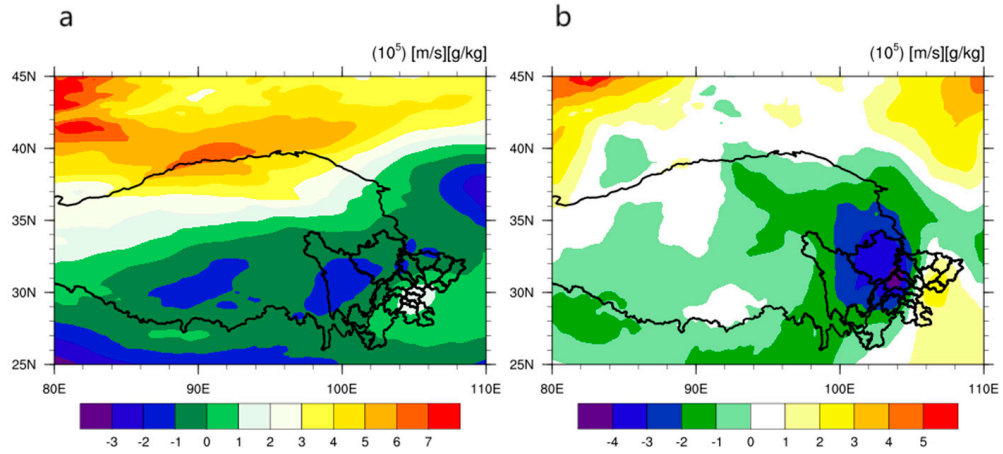


Figure 9. Radial and latitudinal mean water vapour flux maps ((**a**) the latitudinal mean water vapour flux map; (**b**) the radial mean water vapour flux map).

Figure 9b shows the radial distribution of water vapour flux over the observed range, which was not as continuous as the distribution in the latitudinal plot, and the total water vapour flux latitudinal distribution was slightly larger than the radial distribution, with a difference of 1.09×10^5 m s^{-1} g kg^{-1}. The radial distribution of water vapour flux was negative in the range 27° N~37° N, 98° E~103° E, and especially in the range 28° N~35° N, 99° E~103° E, which was a strong negative region, with its maximum reaching about -4×105 m s^{-1} g kg^{-1} at 102° E. This indicates that water vapour was being transported southwards and that it was able to provide a constant supply needed for precipitation in the area of precipitation. The radial distribution of water vapour flux had a wider range than the latitudinal distribution and showed an increasing trend from west to east.

Since 90% of the water vapour was concentrated below 500 hpa, and some of the water that reached 500 hpa lifted and condensed to form clouds, Figure 10 plots the distribution of water vapour flux dispersion at 500 hpa and 700 hpa. Negative values of water vapour flux dispersion mean that water vapour was converging at this location, and positive values mean that it was diverging. The east-central and eastern margins of the Tibetan Plateau at 700 hpa were mainly influenced by the warm and humid airflow from the south and southwest, and most of the water vapour flux dispersion lay in the range of about -2~2 kg/(m^2·s·hpa). There was convective activity in the western Sichuan Basin between 102° E and 106° E, with weak convergent movement of water vapour. Some parts of the north-central Tibetan Plateau were undergoing irradiation of water vapour, with more pronounced irradiation of water vapour in the range of 36° N~38° N, 95° E~97° E, with a value of about -6 kg/(m^2·s·hPa). At 500 hpa, in agreement with 700 hpa, most of the area lay within the water vapour flux dispersion at around -2 to 2 kg/(m^2·s·hPa), while the water vapour convergence zone decreased. In the Sichuan Basin, there was water vapour convergence motion in the range of 31° N~33° N, 102° E~106° E, which was basically the same as the range of the cyclone convergence area shown in Figure 4, but it was reduced compared with the range of 700 hpa water vapour convergence, with its central value around -4 kg m^{-1}s^{-1}. Overall, the water vapour convergence zone for this precipitation process was mainly located in the central and western parts of the Sichuan Basin.

3.5. Comparison of WRF Numerical Simulation Results for Precipitation

Figure 11a shows the simulated low-level horizontal wind field and maximum vertical updraft velocity distribution on 15–16 July, and Figure 11b shows the water vapour mixing ratio and water vapour flux dispersion. The southwestern part of the region was found to have a large south-westerly flow that can bring water vapour. From the specific humidity and water vapour flux scatter plots, it can be seen that the water vapour convergence zone was basically consistent with the zone of large specific humidity values. At Emeishan

Station, the water vapour flux dispersion was negative, and the average specific humidity was able to be up to more than 7 g/kg, wherein water vapour converged and provided water vapour conditions for precipitation. In the airflow convergence, the rising speed was large, up to 0.9 m/s; in the wind field map, we can see the airflow convergence, which provided the rising conditions for precipitation. From the results of this simulation analysis, the simulation was shown to be more successful.

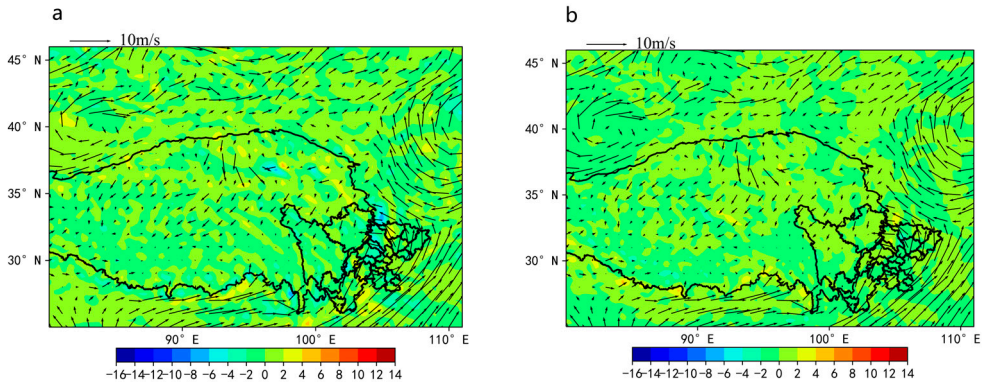


Figure 10. The 700 hpa and 500 hpa wind field and water vapour flux dispersion diagrams ((**a**) 700 hpa wind field and water vapour flux dispersion diagram; (**b**) 500 hpa wind field and water vapour flux dispersion diagram; vector arrows in m/s; colour-filled graph in 10×10^{-4} kg/(m^2·s·hPa)).

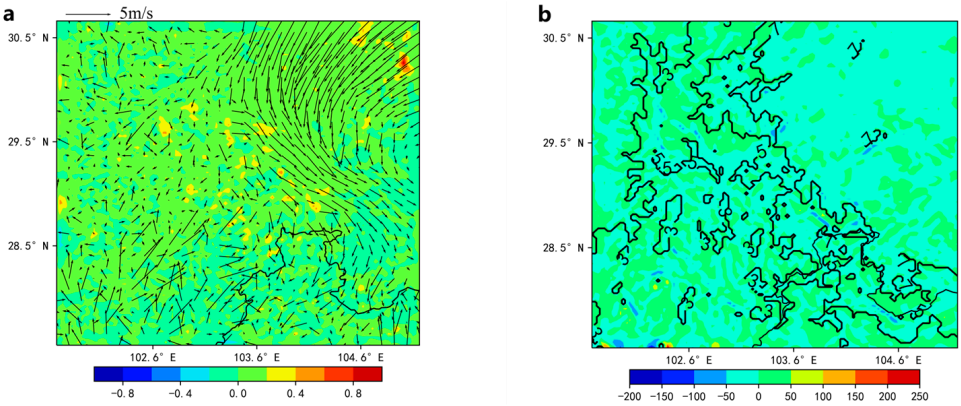


Figure 11. (**a**) is a map of the distribution of the low-level wind field (arrows; units:m/s) and the maximum rate of ascent (filled graph; units:m/s) for the simulation of 15–16 July. (**b**) is a map of the distribution of mean specific humidity (contours; units:g/kg) and water vapour flux dispersion (filled graph; units: 10×10^{-6} kg/(m^2·s)).

Figure 12 shows the cumulative precipitation map of CMORPH precipitation data and WRF d02 simulated precipitation from 00:00 on the 15th to 23:00 on the 16th. From the figure, it can be seen that there was a precipitation high value area in the CMORPH precipitation area, and the precipitation centre at 104° E was roughly simulated. The precipitation high value area simulated by WRF was consistent with the high rising speed area shown in Figure 11a, but the cumulative precipitation simulated in the high precipitation area was larger than that in CMORPH. Regions with precipitation less than 160 mm were well simulated. From the overall results of the simulation, this WRF-simulated precipitation was on the large side compared to CMORPH, and the approximate fallout zones of precipitation and areas of large values of precipitation were better simulated.

Figure 13 shows the hourly precipitation of ERA5 and WRF numerical models at 48 h at Emeishan Station. The precipitation peaked at 00:00, 07:00, and 21:00 on the 15th and at 09:00 on the 16th. The WRF simulation results basically simulated the daily change characteristics of this precipitation, but the time of the peak occurrence was somewhat

different from that of the ERA5 precipitation. Similar to those shown in Figure 12, the simulation results better simulated the precipitation at low values of precipitation and better simulated the precipitation at peak values. It can be seen that this cloud microphysics scheme was biased towards simulating the precipitation at Mount Emei.

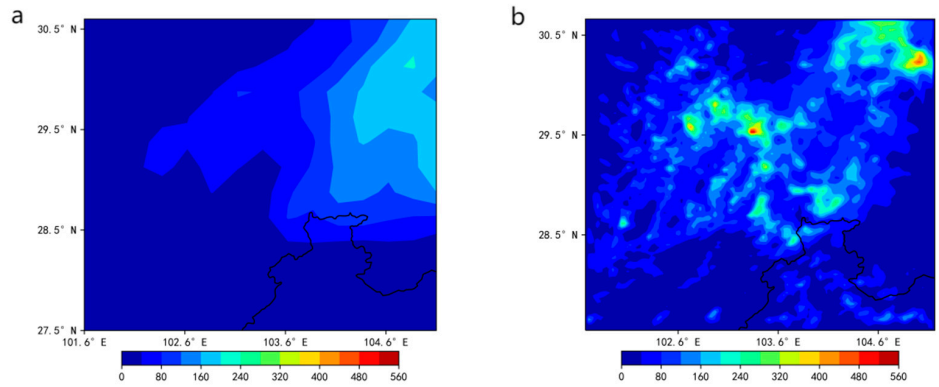


Figure 12. The 48 h cumulative precipitation map from the 15th to the 16th ((**a**) the CMORPH precipitation map; (**b**) the WRF simulated precipitation map, unit: mm).

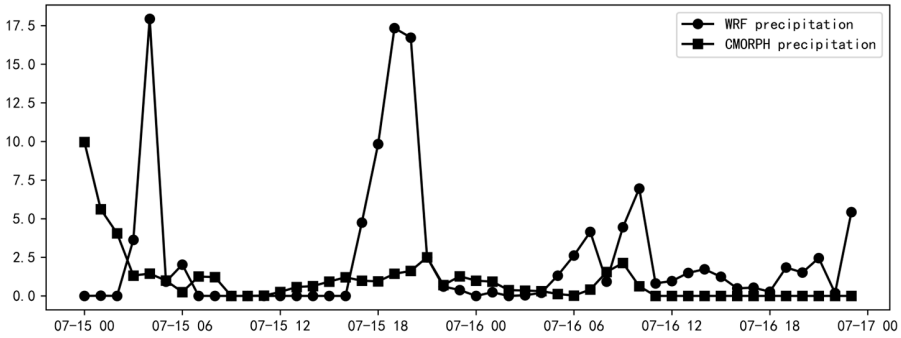


Figure 13. Hourly precipitation of CMORPH data and WRF numerical model at Emeishan Station from 15 to 16 July 2021.

3.6. Sources of Water Vapour Transport

In order to further understand the water vapour source and water vapour distribution at the observation sites, as well as to deepen the understanding of the southwest vortex, this paper simulated the backward trajectory maps of Linzhi Station on 15 July 2021 at three altitudes of 1000 m, 1500 m, and 3000 m, with the time-step of 240 h, using the Hysplit model, as well as the backward trajectory map of Emeishan Station on 15 July 2021 at three altitudes of 500 m, 1000 m, and 1500 m, with a time step of 240 h, and the backward trajectory maps of Naqu and Yushu stations on 15 July 2021 at three altitudes of 100 m, 500 m, and 1000 m, with a time step of 240 h, where the black pentagrams represent the stations.

As shown in Figure 14a, the green trajectory is the dry air with obvious subsidence movement below 400 hpa, the blue and red trajectories are the dry air rising with time fluctuation, and the blue and green trajectories indicate that the main source of water vapour transport in these two altitudes is the water vapour from the Bay of Bengal in the southwest direction. The transport path of water vapour in the red track was westward to the northern part of the Indian Peninsula and then eastward towards Linzhi Station. Between 12 and 13 July, the dry air in the green track was in a sinking motion, while the blue track and the red track were in an ascending motion, and since then, the dry air in the red track was dominant.

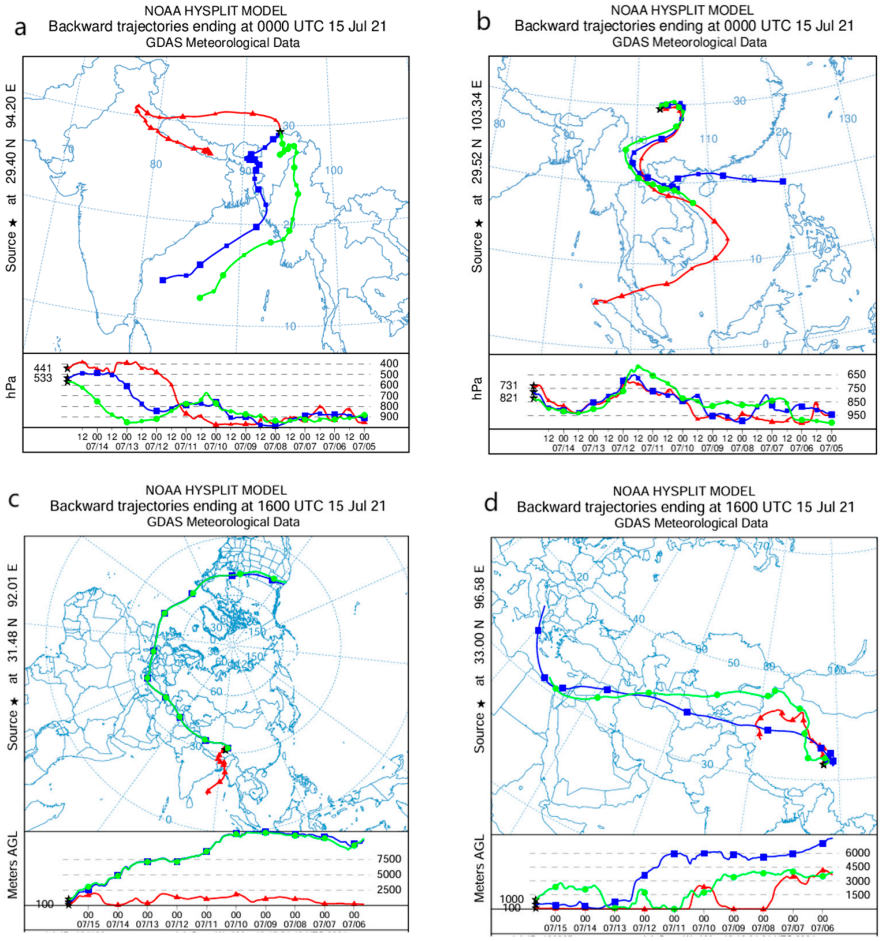


Figure 14. Backward trajectories of 1000 m, 1500 m, and 3000 m at 240 h on 15 July 2021 for Linzhi Station; 500 m, 1000 m, and 1500 m at 240 h on 15 July 2021 for Emeishan Station; and 100 m, 500 m, and 1000 m at 240 h on 15 July 2021 for Yushu Station and Naqu Station (The black five-pointed star in the figure represents the station, and the different coloured lines represent the different water vapour transport channels. (**a**) Linzhi Station; (**b**) Emeishan Station; (**c**) Naqu Station; (**d**) Yushu Station).

From Figure 14b, it can be seen that Emeishan Station was mainly affected by water vapour from the southern Bay of Bengal and the South China Sea, and the water vapour on the red track crossed the Malay Peninsula from the southern Bay of Bengal and was transported through the South China Sea area to Emeishan Station, while the source of the blue and green tracks was water vapour from the South China Sea in the southeast direction. All three tracks fluctuated upward from 0:00 on 5 July to 12:00 on 12 July, with the green track dominating most of the time from 12:00 on 6 July until 12:00 on 12 July, after which the dry air in all three tracks sank rapidly and began to rise again by 14 July. The source of water vapour at Naqu Station as shown in Figure 14c was not only from the Bay of Bengal in the south but also from the Pacific Ocean in the western hemisphere, and the dry air at both 1000 m and 500 m was in a slow sinking motion.

The source of water vapour at Yushu Station is shown in Figure 14d to be mainly from the northwestern European range, and at the 100 m altitude level was mainly from the northwestern part of the country. The air on all three trajectories was in a fluctuating and sinking motion before 13 July, with the blue trajectory dominating and the green trajectory rising rapidly and then sinking rapidly after 13 July. Based on the above analysis, it was found that the analysis results of Li et al. [37] on the water vapour transport characteristics in the southeastern region of the Qinghai Tibet Plateau were relatively consistent. During the monsoon period, there was mainly southwest airflow in the lower layer, and the water vapour transport channel height of the western airflow was higher than 3000 m, while the water vapour transport channel height of the southwest and southeast airflow was about 2000 m.

From Figure 15a, it can be seen that the source of water vapour at 1500 m altitude for both Linzhi Station and Emeishan Station was the Bay of Bengal in the southwest, and the red trajectory transported water vapour from the Bay of Bengal through the South China Sea to Emeishan Station, with there being an intersection of the two trajectories at 10 o'clock on 12 July, after which the air in the red trajectory sunk rapidly, and the air in the blue trajectory rose rapidly. In order to better understand the source and contribution of water vapour at Emeishan Station, this paper applied the Meteinfo model to cluster the water vapour sources at the 1500 m altitude layer of Emeishan Station for 72 h and selected the six trajectories with the most important contribution, as shown in Figure 15b, where the red triangles indicate Emeishan Station and the trajectories with different colours represent the water vapour sources from different directions. The largest contribution was the blue trajectory from the Sichuan Basin in the northeast direction, with a contribution of 28.79%, followed by the yellow trajectory from Guizhou in the southwest direction with a contribution of 27.65%, and water vapour transport from the purple trajectory from the Sichuan Basin in the southwest direction with a contribution of 24.62%, as well as from the purple-red trajectory from the southeast direction with a contribution of 10.23% and the green trajectory with a contribution of 5.3%. Therefore, the source of water vapour transport at Emeishan Station on 15 July 2021 was mainly in the two ranges of the Sichuan Basin and the southwestern direction.

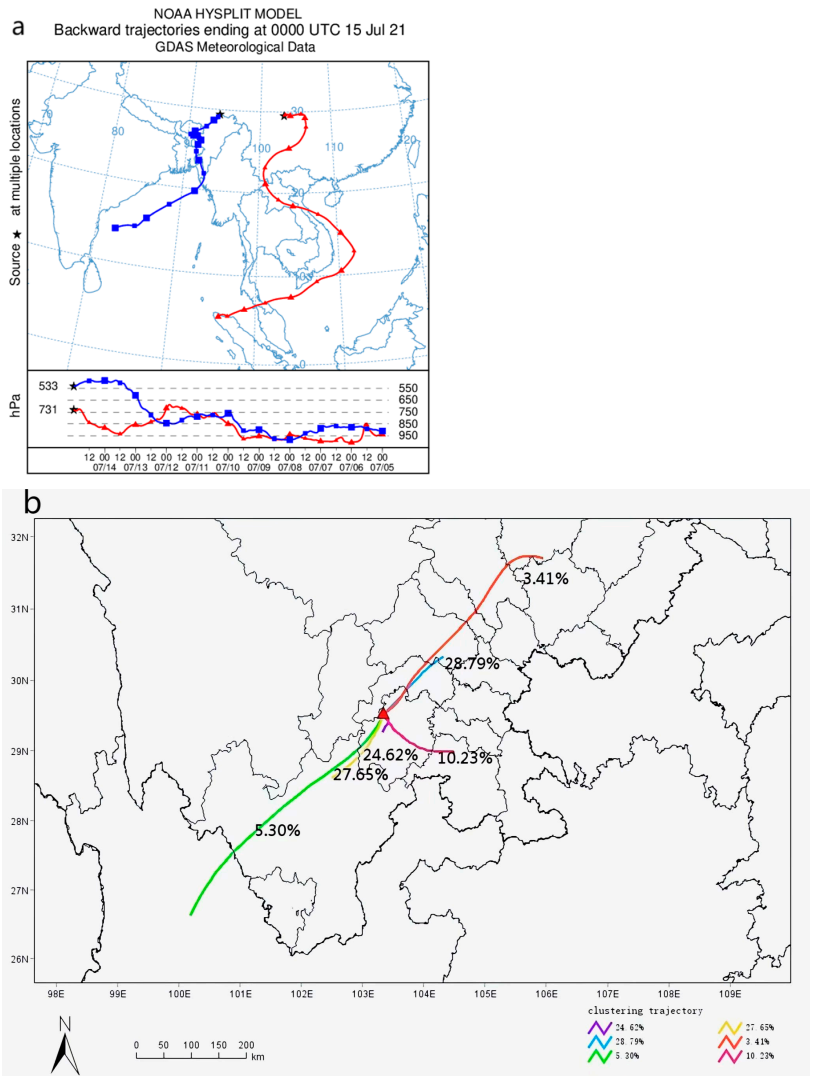


Figure 15. Backward trajectory plot of 1500 m at 240 h on 15 July 2021 for Linzhi and Emeishan stations, as well as a cluster analysis plot of 1500 m at 72 h on 15 July 2021 at Emeishan Station (The

black pentagram in figure a and the red triangular star in figure b both represent stations. (**a**) the backward trajectory plot, where the blue trajectory is for Linzhi Station and the red trajectory is for Emeishan Station; (**b**) the cluster analysis plot).

4. Summary and Conclusions

This study analysed a specific case of a southwest vortex precipitation event that occurred on 15–16 July 2021, focusing on the characteristics of atmospheric motion and water vapour transport. Combining the analysis of raindrop spectra observed at the Emei Mountain station, the study draws the following conclusions:

(1) Influenced by the southwest vortex, the precipitation at Emeishan Station exhibited higher rain intensity and volume. The raindrop spectral distribution was notably wide, presenting a bimodal structure. Among the three types of precipitation clouds, stratiform clouds had the largest peak number concentration and better gamma fit. Precipitation particles of small size contributed the most to precipitation.

(2) The heavy rainfall event resulted from the interplay between the low-level southwest vortex over the Sichuan Basin and the high-level South Asian high-pressure system, leading to a weather situation characterised by upper-level divergence and low-level convergence. Conditions such as atmospheric thermal stratification instability in the lower and middle layers, a significant vertical uplift rate, substantial water vapour, and the presence of water vapour convergence movements during the precipitation of the southwestern vortex provided important support for the strengthening and persistence of the southwestern vortex.

(3) The WRF simulation of heavy rainfall caused by the southwest vortex was successful in accurately modelling the precipitation fallout area and regions with intense precipitation, despite the estimated precipitation values being somewhat high. Future improvements could include refining the simulation through triple nesting or altering the cloud microphysics parameterisation scheme to better replicate southwest vortex precipitation events and align model output more closely with actual observations.

(4) The Sichuan Basin experienced two primary moisture transport paths during the southwest vortex event: channel 1 comes from the Bay of Bengal and reaches the Sichuan Basin through the South China Sea; channel 2 originates from the water vapour transported directly from the South China Sea. Contributions from the southwest part of the basin accounted for 57.57% of the moisture. In the Qinghai–Tibet Plateau region, there are three moisture transport sources: the Bay of Bengal, moisture transported westward from the western Pacific in the Western Hemisphere, and moisture transported westward from the northwestern part of Europe.

By analysing the weather situation of the southwest vortex, the average vorticity in the mid-lower troposphere, vertical motion speed, and moisture distribution, it was demonstrated that the large-scale environmental field provides favourable conditions for the formation of the southwest vortex. Several important factors and conditions contributing to the development and persistence of the southwest vortex were identified. Through backward trajectory analysis of four stations in the region, the main sources and pathways of moisture transport during the southwest vortex period were determined.

Author Contributions: T.W., M.G. and M.L. were mainly responsible for writing the manuscript, research design, and data analysis. M.L., Y.M. and F.S. were responsible for overseeing the progress of the study and revising the manuscript. M.G. and M.L. were responsible for the design of the research methodology and the analysis of the backward trajectories. Y.L., Y.J. and P.X. were responsible for acquiring data and ensuring data quality. All authors have read and agreed to the published version of the manuscript.

Funding: This work was financially supported by the Second Tibetan Plateau Scientific Expedition and Research (STEP) program (grant no. 2019QZKK0103), and the Natural Science Foundation of Sichuan Province (grant no. 2022NSFSC0217).

Data Availability Statement: The European Centre for Medium-Range Weather Forecasts ERA5 reanalysis information (https://cds.climate.copernicus.eu/cdsapp#!/search?type=dataset, accessed on 18 January 2024 and 14 March 2023). The global data assessment system (GDAS) data were obtained from the National Centers for Environmental Prediction (NCEP) of the United States (https://www.ready.noaa.gov/gdas1.php, accessed on 10 January 2023). National Centres for Environmental Prediction (NECP)/National Center for Atmospheric Research (NCAR) FNL 1° × 1° reanalysis data at 6 h intervals (https://rda.ucar.edu/datasets/ds083.2/dataaccess/#, accessed on 24 January 2024). Climate Prediction Center (CPC) global high temporal and spatial resolution CMORPH precipitation data (https://www.ncei.noaa.gov/products/climate-data-records/precipitation-cmorph, accessed on 29 January 2024). Raindrop spectral data from the Emei Mountain Integrated Atmosphere and Environment Observation Experiment Station, Chengdu University of Information Engineering (data are not publicly available as they are from school observatories).

Acknowledgments: This work was financially supported by the Second Tibetan Plateau Scientific Expedition and Research (STEP) program (grant no. 2019QZKK0103), the National Natural Science Foundation of China (grant no. 42230610), the Natural Science Foundation of Sichuan Province (grant no. 2022NSFSC0217), and the Scientific Research Project of Chengdu University of Information Technology (KYTZ201721).

Conflicts of Interest: The authors declare no conflicts of interest.

References

1. Kang, L.; Hao, L.P.; Niu, J.L. Characterisation of the southwestern low vortex that triggers heavy rainfall. *Plateau Meteorol.* **2011**, *30*, 1435–1443.
2. Li, G.P. *Dynamical Meteorology of the Tibetan Plateau*, 2nd ed.; Meteorological Press: Beijing, China, 2007.
3. Lu, J.H. *Introduction to Southwest Low Vortex*; Meteorological Press: Beijing, China, 1986.
4. Chen, Y.R.; Li, Y.Q.; Zhao, T.L. Cause Analysis on Eastward Movement of Southwest China Vortex and Its Induced Heavy Rainfall in South China. *Adv. Meteorol.* **2015**, *2015*, 1–22. [CrossRef]
5. He, G.B. Review of the Southwest Vortex Research. *Meteorol. Mon.* **2012**, *38*, 155–163.
6. Mao, Z.Y.; Liu, J.Q. Classification of rainstorms in Hunan Province affected by the Southwest China vortex. *J. Torrential Rain and Disasters.* **2021**, *40*, 52–60.
7. Zhao, W.L.; Feng, X.Y.; Wang, S.G.; Su, Q.F.; Luo, B.; Du, Y.S.; Han, J.J.; Hu, Y.L. Comparative Study on Atmospheric Environment Effects of Cases of Dry and Wet Southwest Vortices in Sichuan Basin. *Plateau Meteorol.* **2020**, *39*, 130–142.
8. Gao, S.; Chen, G.C.; Wu, Z.; Du, Q.; Zhao, L.; Huyan, L. A case analysis of rainstorm in Sichuan—Chongqing region under the influence of a southwest vortex. *J. Arid Meteorol.* **2019**, *37*, 597–612.
9. Tu, N.N.; Li, Y.Q. A Case Analysis of Southwest Vortex Causing Heavy Rainfall in Eastern Sichuan. *J. Arid Meteorol.* **2014**, *32*, 962–971.
10. Wang, Z.S.; Wang, Y.H.; Liang, Y.G. Numerical experiments on a heavy rainfall caused by southwest vortex. In *A Study on the Rainstorm Science, Operational Experiments and Theory of Weather Dynamics*; China Meteorological Press: Beijing, China, 1996; pp. 257–267. (in Chinese)
11. Bao, C.L. A case study of a southwestern vortex developing into a typhoon in the South China Sea. *Acta Meteorol. Sin.* **1981**, *1*, 123–127. [CrossRef]
12. Tao, S.Y. *Rainstorms in China*; Meteorological Press: Beijing, China, 1980.
13. Li, Y.Q. New Related Progress on Researches of the Vortex Source of Southwest China Vortex. *Plateau Meteorol.* **2021**, *40*, 1394–1406. [CrossRef]
14. Lai, X.; Wang, Q.Y.; HuangFu, J.L.; Jiang, X.W.; Wang, L.; Chen, W.; Huang, R.H.; Fu, S.M.; Cen, S.X.; Tang, Y.L. Progress in Climatological Research on the Southwest China Vortex. *Chin. J. Atmos. Sci.* **2023**, *47*, 1983–2000. (In Chinese) [CrossRef]
15. Zhong, X.H.; Song, P.L.; Lv, X.P. An analysis of individual cases of large rainstorms in Xinxiang City. *Henan Meteorol.* **1999**, *4*, 4,19–20.
16. Liu, J.Q.; Li, Z.L. A Case Study of a Heavy Rainstorm in Hunan Triggered by the Induced Cyclone of Southwest Vortex. *Plateau Meteorol.* **2020**, *39*, 311–320. [CrossRef]
17. Huang, H.L.; Li, L. A Synchronous Variation Process of Tibetan Plateau Vortex and Southwest Vortex. *J. Appl. Meteorol. Sci.* **2023**, *34*, 451–462.
18. Wang, X.M.; Liu, Y. Causes of extreme rainfall in May 2013 over Henan Province: The role of the Southwest vortex and low-level jet. *Theor. Appl. Climatol.* **2017**, *129*, 701–709. [CrossRef]
19. Chen, Z.M.; Min, W.B.; Miao, Q.; He, G.B. A Case Study on Coupling Interaction between Plateau and Southwest Vortexes. *Plateau Meteorol.* **2004**, *23*, 75–80. [CrossRef]
20. Deng, C.Z.; Zhao, Y.; Kong, F.Y.; Zhai, D.H.; Li, Q.; He, Y. A Numerical Simulation Study of the Southwest Vortex Mechanism during the "6·30" Heavy Rain Event in Sichuan and Chongqing. *Plateau Meteorol.* **2021**, *40*, 85–97. [CrossRef]

21. Gao, W.L.; Yu, S.H. The Case Study in Causes and Environmental Fields Analysis of Departure Plateau Vortex Accompanying with Induced Southwest Vortex. *Plateau Meteorol.* **2018**, *37*, 54–67. [CrossRef]
22. Cheng, X.L.; Li, Y.Q.; Xu, X.D.; Heng, Z.W. Research and Numerical Simulation of a Torrential Rain Caused by the Southwest China Vortex during Flood Period. *Plateau Meteorol.* **2019**, *38*, 359–367.
23. Jiang, L.X.; Chen, K.Y.; Wang, L.S.; Li, D.Y. Study of the Impact of the Assimilation of FY3C Microwave Humidity Sensor-2 Data on a Case of the Numerical Simulation of the Southwest China Vortex-induced Rainstorm. *Plateau Mt. Meteorol. Res.* **2021**, *41*, 18–24. [CrossRef]
24. Lu, P.; Li, Y.Q. Simulation of Effect of Subtropical High Enhancement on Southwest Vortex. *Chin. J. Atmos. Sci.* **2021**, *45*, 851–862. [CrossRef]
25. Li, L.; Zhang, R.H.; Wen, M. Genesis of southwest vortices and its relation to Tibetan Plateau vortices. *Q. J. R. Meteorol. Soc.* **2017**, *143*, 2556–2566. [CrossRef]
26. Zwiebel, J.; Baelen, J.V.; Anquetin, S.; Pointin, Y.; Boudevillain, B. Impacts of orography and rain intensity on rainfall structure. The case of the HyMeX IOP7a event. *Q. J. R. Meteorol. Soc.* **2016**, *142*, 310–319. [CrossRef]
27. Yang, J.M.; Chen, B.J.; Han, Y.X.; Li, P.R. Statistical characteristics of raindrop size distribution in different regions of Shanxi. *J. Meteorol. Sci.* **2016**, *36*, 88–95.
28. Chang, Y.; Guo, X.L. Characteristics of convective cloud and precipitation during summer time at Naqu over Tibetan Plateau. *Chin. Sci. Bull.* **2016**, *61*, 1706–1720. [CrossRef]
29. Gong, M.; Li, M.S.; Shu, L.; Chang, N.; Xu, P.; Ma, Y.; Sun, F.; Yang, Y. Microphysical Analysis of Precipitation in the Central and Eastern Margins of the Tibetan Plateau. *Atmosphere* **2022**, *13*, 1082. [CrossRef]
30. Xu, Y.H.; Wang, Z.D.; Wang, M. *Climate of Southwest China*; Meteorological Press: Beijing, China, 1991.
31. Wang, H.; Tan, L.; Zhang, F.; Liu, Y.; Zeng, Q.; Yan, Y.; Ren, X.; Xiang, J. Three-Dimensional Structure Analysis and Droplet Spectrum Characteristics of Southwest Vortex Precipitation System Based on GPM-DPR. *Remote Sens.* **2022**, *14*, 4063. [CrossRef]
32. Liu, Z.; Wu, X.Y.; Yu, Y.; Ren, Z.H. Analysis on raindrop size distribution of typical stations in China during rainy season. *Hubei Agric. Sci.* **2021**, *60*, 53. [CrossRef]
33. Chang, N.; Li, M.S.; Wang, L.Z.; Gong, M.; Fu, W.; Shu, L. Study on Micrometeorological Characteristics of Near Surface Layer in Emeishan Area. *Plateau Meteorol.* **2022**, *41*, 226–240. [CrossRef]
34. Yu, J.Y.; Li, M.S.; Yin, S.C.; Lv, Z.; Song, X.Y. Analysis of Cloud Precipitation Microscopic Characteristic Raindrop Spectrum in Naqu Area of Qinghai-Tibet Plateau. *J. Chengdu Univ. Inf. Technol.* **2020**, *35*, 188–194. [CrossRef]
35. Shu, L.; Li, M.S.; Hua, S.; Suolang, J.C.; Lv, Z.; Fu, W.; Wang, L.Z.; Yin, S.C. Statistical Characteristics of Raindrop Size Distribution and Microphysical Structure of Cloud in Yushu Region of Qinghai Tibet Plateau. *Adv. Meteorol. Sci. Technol.* **2021**, *11*, 113–121.
36. Sun, B.; Zhu, Y.L.; Wang, H.J. The recent interdecadal and interannual variation of water vapor transport over eastern China. *Adv. Atmos. Sci.* **2011**, *28*, 1039–1048. [CrossRef]
37. Li, M.S.; Wang, L.Z.; Chang, N. Characteristics of the Water Vapor Transport in the Canyon Area of the Southeastern Tibetan Plateau. *Water* **2021**, *13*, 3620. [CrossRef]

Disclaimer/Publisher's Note: The statements, opinions and data contained in all publications are solely those of the individual author(s) and contributor(s) and not of MDPI and/or the editor(s). MDPI and/or the editor(s) disclaim responsibility for any injury to people or property resulting from any ideas, methods, instructions or products referred to in the content.